R4-B.2: Multi-Energy, Limited-View Computed Tomography

I. PARTICIPANTS INVOLVED FROM JULY 1, 2019 TO JUNE 30, 2020

Faculty/Staff			
Name	**Title**	**Institution**	**Email**
Eric Miller	PI	Tufts University	eric.miller@tufts.edu
James Webber	Postdoctoral Researcher	Tufts University	James.webber@tufts.edu
Kenny Yau	Research Engineer	Tufts University	Kenny.Yau@tufts.edu

II. PROJECT DESCRIPTION

A. Project Overview

A.1. X-Ray Modeling and Processing

The development of new scanning technologies by Rapiscan Systems has led to the analysis of novel integral transforms and inversion methods in Bragg Scattering Tomography (BST) and Compton Scattering Tomography (CST). The advances made by the teams at Tufts and Rapiscan Systems this year lay the groundwork for better material characterizations and for modification of the currently employed threat detection algorithms, with the ultimate goal to improve the false alarm rates.

Our specific focus was on a Real Time Tomography (RTT) X-ray portal scanner, with the ability to measure simultaneously Bragg scatter, Compton scatter, and transmission (X-ray CT) data. Our aim was to successfully fuse the multiple data streams to enhance the image quality and threat classification accuracy. The square tunnel geometry, collimation technology, and energy sensitive capabilities of the scanner were shown to be crucial to the mathematical analysis and inversion. In particular, we derived explicit inversion formulae for the BST and CST transforms in the RTT geometry. The inversion techniques presented give a fast, analytic means to process the Bragg and Compton signal in order to recover the material properties (e.g., the crystalline structure and electron density of the items present in the image). Knowledge of such material characteristics helps us to better distinguish threat and nonthreat materials, and hence we anticipate that our methods will offer a reduction in the false alarm rates moving forward.

We considered the joint reconstruction of the electron density and attenuation coefficient using Compton and transmission data, with the aim to enhance the edge recovery of both images simultaneously, and to more precisely localize the image space for suspected threats. Our results showed great promise on simulated phantoms.

Following our work in Year 6, we completed the development of a Monte Carlo (MC) MATLAB package for the simulation of the Bragg, Compton, and Rayleigh processes. In Year 7, we set out to verify our BST and CST inversion methods using MC data. The MC code was also applied to simulate data acquisition scenarios of interest to Rapiscan (e.g., to simulate energy histograms and photon counts).

A.2. Optical Image Processing

Trace chemical identification on a surface has important applications, for example in security and forensics in identifying illicit drugs and explosives [1, 2]. The traditional process of bringing a sample to a lab for identification is costly in terms of time and money, not only adding a financial burden but also delaying decisions that require the desired information. While not as powerful as their laboratory counterparts, portable spectrometers capable of trace detection such as those discussed in [3-5] have exhibited adequate performance to enable them to fill a gap in on-site spectroscopy technology. To the best of our knowledge, existing products and technologies still require constant user interaction to scan a surface region for potential threat particles and initiate analyses of said particles.

Tufts University collaborated with Pendar Technologies. The company has expertise in the portable Raman spectrometer domain to address this autonomous technology gap. The project was called the Portable Chemical Fingerprint Identification System (PCFIS).

The goal of the PCFIS project was to create a device that adds autonomous functionality to existing portable microscopy capabilities. Specifically, we wanted to *automatically* scan a $1'' \times 1''$ region of a surface, in general not flat, for potential threat particles; *automatically* analyze the composition of a subset of the potential threats, the number of which is user-specified; and *automatically* provide an image that sharply resolves the entirety of the $1'' \times 1''$ region, called a "flattened image."

The Tufts team focused on the optical image processing necessary for automatically finding potential threat particles and for facilitating Raman spectroscopy. These included a topography estimation algorithm of the $1'' \times 1''$ region using a focal stack of a particular scene; a fast method of producing a large depth-of-field image from the focal stack; a particle detection algorithm that is robust against slowly varying background illumination; and an aim assist algorithm for the device to properly focus the Raman laser beam onto the particle being analyzed. The prototype was able to automatically scan a $1'' \times 1''$ region for particles and analyze the composition of 10–20 particles in 3–5 minutes.

B. State of the Art and Technical Approach

B.1. X-Ray Modeling and Processing

The RTT portal scanner geometry, under principle consideration by the Tufts team this year, is displayed in Figure 1. The scanner sources (with coordinate $\mathbf{s}$) are fixed and switched along the linear array $\{x_2 = -1, x_3 = 0\}$. The sources are assumed to be polychromatic and approximately 2-D fan-beam (in the (x_1, x_2) plane), with opening angle β. The forward scatter (Bragg) detectors (with coordinate $\mathbf{d}_B$) are assumed to be energy-resolved and lie on the $\{x_2 = 1\}$ plane, with small (relative to the scanning tunnel size) offset ϵ in the x_3 direction. The detectors are collimated to record photons that scatter on planes in $\mathbb{R}^3$ (see Figure 1b), where the planes of collimation are orientated to intersect the source (x_1, x_2) plane along horizontal lines (parallel to x_1). Hence the Bragg photon arrivals measured by the portal scanner detectors are scattered from horizontal lines embedded in the (x_1, x_2) plane. An example line of intersection is illustrated by L in Figure 1. The backscatter (Compton) detectors (with coordinate $\mathbf{d}_C$) are located on $\{x_2 = -0.8\}$. They are energy-resolved and uncollimated, allowing for photon arrivals in all directions. The forward (transmission) detectors (with coordinate $\mathbf{d}_A$) lie on the line $\{x_2 = 1, x_3 = 0\}$, and measure the intensity of unattenuated photons.

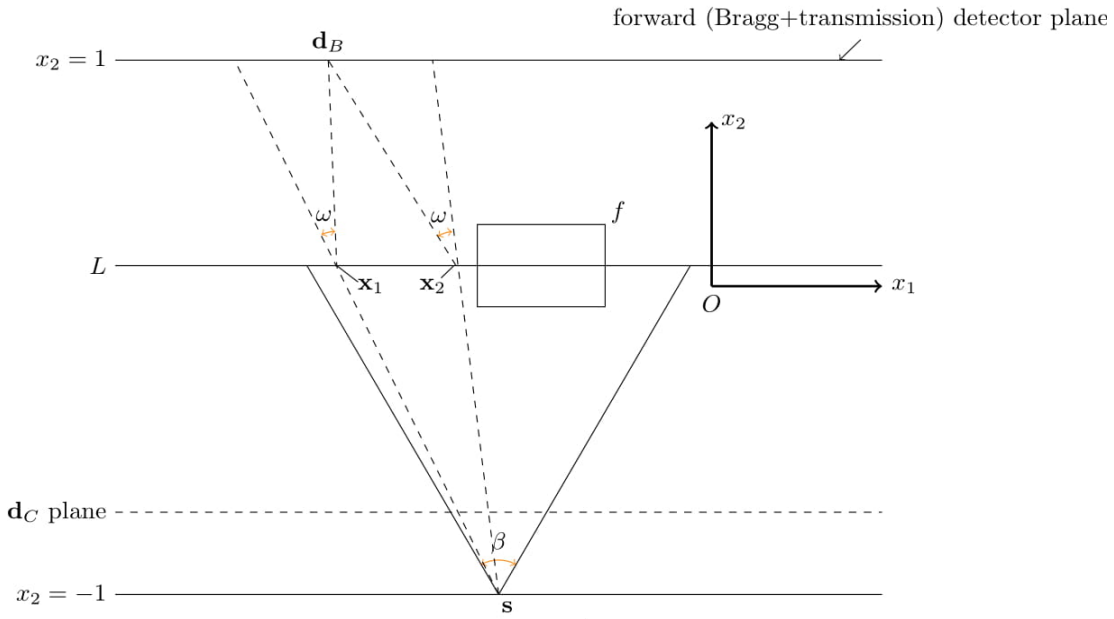

Figure 1a: (x_1, x_2) (source fan-beam) plane cross-section. The source(s) opening angle is β and we have shown two scattering locations at $x_1, x_2 \in L$ with scattering angle ω.

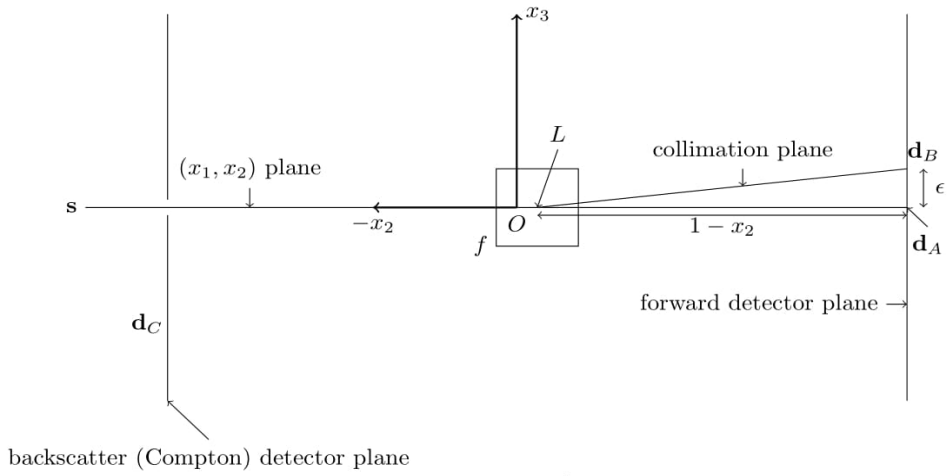

Figure 1b: (x_2, x_3) plane cross-section. Note that L is now orthogonal to the page (parallel to x_1).

Figure 1: The RTT portal scanner geometry. The scanned object is labelled by f. The detectors are collimated to planes, and the scattering events occur along lines $L = \{x_2 = a, x_3 = 0\}$, for some $-1 < a < 1$. The Bragg scatter from L is measured by detectors $\mathbf{d}_B \in \{x_2 = 1, x_3 = \epsilon\}$, for some $\epsilon > 0$. The Compton backscatter is measured by $\mathbf{d}_C \in \{x_2 = -0.8\}$, and the transmission data is measured by $d_A \in \{x_2 = 1, x_3 = 0\}$.

Let $\boldsymbol{x} = (x_1, x_2)$. Then the data streams collected by the RTT are modelled as follows:

1. Transmission—the intensity of unattenuated photons $I_A(E, \mathbf{s}, \mathbf{d}_A)$ is described by the Beer-Lambert law [6]

$$\log \frac{I_0(E)}{I_A(E, \mathbf{s}, \mathbf{d}_A)} = R\mu_E(E, \mathbf{s}, \mathbf{d}_A) = \int_{l_{\mathbf{s},\mathbf{d}_A}} \mu_E(\boldsymbol{x})\, \mathbf{d}\boldsymbol{x},$$

   where $\mathrm{I}_0(\mathrm{E})$ is the initial source intensity and μ_E is the attenuation coefficient at energy E. The integrals are taken over lines $\mathrm{l}_{\mathrm{s,d_A}}$ connecting $\mathrm{s} \in \{\mathrm{x}_2 = -1, \mathrm{x}_3 = 0\}$ and $\mathrm{d_A} \in \{\mathrm{x}_2 = 1, \mathrm{x}_3 = 0\}$, and the transmission data determines the line Radon transform $\mathrm{R}\mu_\mathrm{E}$ of μ_E [7].

2. Bragg forward scatter—the Bragg intensity $I_B(E, \mathbf{s}, \mathbf{d}_B)$ scattered from powder samples is modelled as integrals of the differential cross section function $F(q, \mathbf{x})$ over C^2 curves [8]

$$I_B(E, \mathbf{s}, \mathbf{d}_\mathrm{B}) = \mathcal{B}F(E, \mathbf{s}, \mathbf{d}_\mathrm{B}) = \int_L F\left(E \sin\frac{\omega(\boldsymbol{x}, \mathbf{s}, \mathbf{d}_\mathrm{B})}{2}, \mathbf{x}\right) \mathbf{dx},$$

   where L is a line parallel to x_1 (as in Figure 1a), $q = E \sin\frac{\omega(\mathbf{x},\mathbf{s},\mathbf{d}_\mathrm{B})}{2} \in \mathbb{R}^+$ is the momentum transfer and $\omega(\mathbf{x}, \mathbf{s}, \mathbf{d}_\mathrm{B}) \in [0, \pi]$ is the scattering angle of the interaction, as pictured in Figure 1a. The Bragg transform $\mathcal{B}$ describes the integrals of a function over the 3-D set of 1-D curves in the plane,

$$\mathcal{Q} = \left\{(q, x_1) \in \mathbb{R}^2 : q = E \sin\frac{\omega(\mathbf{x}, \mathbf{s}, \mathbf{d}_\mathrm{B})}{2}\right\}$$

   for each fixed $x_2 \in (-1,1)$, where $E \in \mathbb{R}^+$, $\mathbf{s} \in \{x_2 = -1, x_3 = 0\}$ and $\mathbf{d}_B \in \{x_2 = 1, x_3 = \epsilon\}$, for some $\epsilon > 0$.

3. Compton backscatter – the intensity of Compton backscattered photons $I_C(E, \mathbf{s}, \mathbf{d}_\mathrm{C})$ is modelled as integrals of the electron density n_e over toric sections [9]

$$I_C(E, \mathbf{s}, \mathbf{d}_\mathrm{C}) = \boldsymbol{\mathcal{T}} n_e(E, \mathbf{s}, \mathbf{d}_\mathrm{C}) = \int_{\boldsymbol{T}(E,\mathbf{s},\mathbf{d}_C)} n_e(\mathbf{x})\, \mathbf{d}x.$$

   A toric section is the union of two intersecting circles with the same radius. Here $\boldsymbol{T}(E, \mathbf{s}, \mathbf{d}_\mathrm{C})$ is the toric section with points of self-intersection at $\mathbf{s}$ and $\mathbf{d}_C$, with radius determined by E, and the Compton data is described by the toric section transform $\boldsymbol{\mathcal{T}} n_e$ of n_e. Geometrically, the CST problem is 2-D and the Compton interactions occur in the (x_1, x_2) plane (in Figure 1a). Note that the dimensions used here are not exactly the same as in [9], but the geometry is analogous.

The modelling of transmission data is well established in the literature [7], and the inversion properties of the Radon transform R are well understood [10]. The novel advances made by the team at Tufts this year are towards the physical modelling of the BST and CST problem, and the inversion and stability properties of the transforms $\boldsymbol{\mathcal{T}}$ and $\mathcal{B}$. We also consider the simultaneous reconstruction of n_e and μ_E from the joint data, $\boldsymbol{\mathcal{T}} n_e$ and $R\mu_E$, to improve the image edge resolution.

Using the theory of [11, 12], in [8] we propose new physical models for the RTT geometry that estimate the Bragg scattered signal from line samples of randomly orientated crystallites (powder scattering). When the effects due to attenuation are ignored, the physical models lead us to a new, linear Radon transform, namely $\mathcal{B}$ (as in 2 above). The removal of attenuation from the modelling is a common assumption made in the scattering tomography literature, for example in Compton Scattering Tomography (CST) [13-15]. While neglecting attenuation introduces a systematic error in the modelling, the linearization of the model allows us to apply the theory of linear integral equations and Radon transforms to obtain an explicit solution. Further the linear analysis will likely shed light on the inversion and stability properties in the nonlinear case (with attenuation included) and provides the theoretical groundwork required to move forward with such problems.

The Bragg transform maps F (the reconstruction target) associated with the crystalline material to its integrals over the set of curves Q, as in 2 above. By exploiting the translational invariance of $\mathcal{B}$, and using the established theory of linear Volterra integral equations [16] and analytic continuation ideas, we prove the injectivity and explicit invertibility of $\mathcal{B}$ in Theorem 4.1 of [8]. We also show that $\mathcal{B}$ is a bounded operator in Corollary 4.4 of [8], in a least squares sense. In more detail, Corollary 4.4 gives bounds for the data magnitude in L^2 (i.e., $\|\mathcal{B}F\|_{L^2}$) in terms of the target magnitude $\|F\|_{L^2}$.

This work lays the foundation for new imaging techniques in Bragg spectroscopy, a decades old idea, dating back to the experiments of Debye-Scherrer [17] and the works of [18], which image the crystal structure of point samples using monochromatic, pencil-beam sources. Our analysis considers the BST problem with polychromatic, fan-beam sources, where the (3-D) crystal sample is observed along lines L. The energy-resolving capabilities of the RTT detectors (a technology not available to [17, 18]) allow us also to distinguish the energies of the spectrum, which adds new dimensionality to the data, and plays a crucial role in the derivation of our main theorems (e.g., in Theorem 4.1 of [8]).

We give an extension of the results of Theorem 4.1 of [8] to three dimensions (and further to n dimensions) in Theorem 5.1 of [8]. In 3-D the Bragg transform models the Bragg signal in the scanning geometry displayed in Figure 2. Here the scattering is restricted to planes of crystallites in $\mathbb{R}^3$. This is analogous to the 2-D case in Figure 1, where the scatter is constrained to lines $L \subseteq \mathbb{R}^2$. We anticipate that the scanning modality of Figure 2 will have practical application in the materials characterization of thin films as on page 150 of [19].

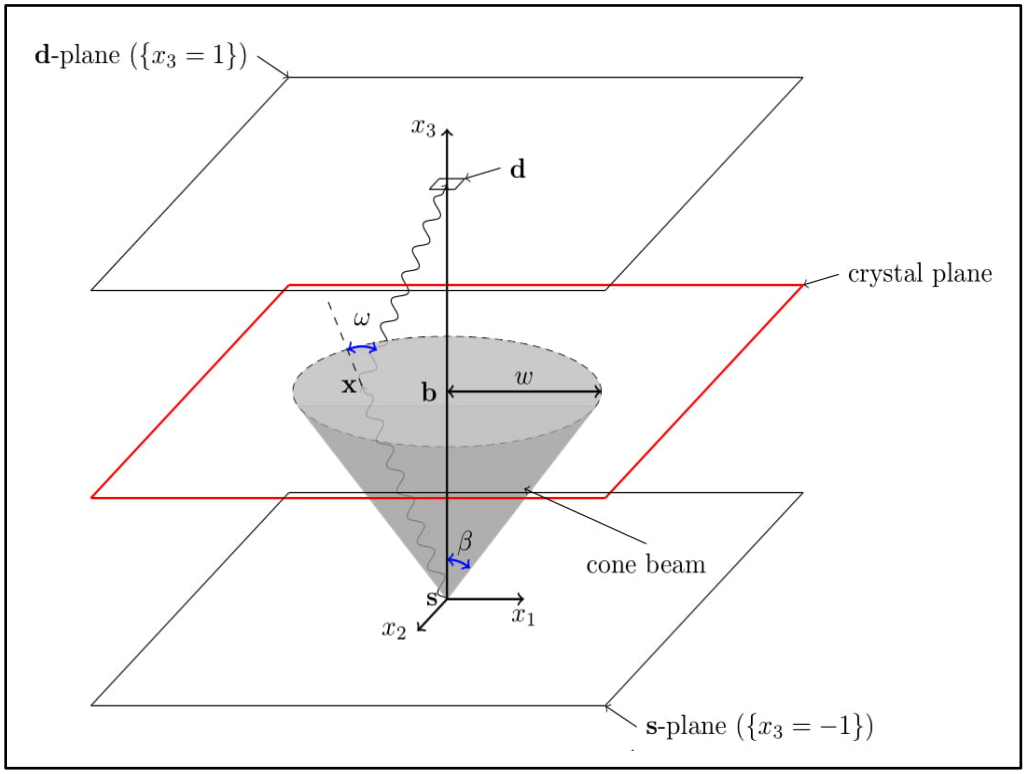

Figure 2: Bragg scanning modality in 3-D. A square detector d is shown opposite a source s, and collects photons (shown as wavy lines) scattered from points x on the crystal plane. The crystal sample (the red plane) is placed between, and is parallel to, the s-plane and d-plane. The center of the base of the cone is b, the source opening angle is β (as in Figure 1), and the source width is $w = |\mathbf{b} - \mathbf{s}|\, tan\, \beta$.

Additionally, in Section 6.2, we use the conditions of our theorems to assist in machine design of the RTT. Roughly speaking, the design condition we derive specifies that the detector offset ϵ not be too large relative to the source fan width $w = (1 - x_2)\tan\beta$ (see Figure 1). Specifically, we provide example detector configurations for varying β, so that the resulting condition is satisfied, thus allowing us to apply the proposed inversion formulae.

In [9] we present new physical models for the CST problem in the RTT geometry, following the theory of [13-15, 20, 21]. We show how the Compton intensity can be approximated by toric section integrals $\mathcal{T}n_e$ of n_e, as in 3 above. As in the Bragg case, the effects due to attenuation are ignored in the CST modelling, which linearizes the forward problem. This allows us to apply linear Radon transforms theory to obtain a closed-form solution for n_e in terms of $\mathcal{T}n_e$. Specifically, by exploiting the translational invariance of the RTT geometry, and using Paley-Wiener-Schwartz theorem ideas, we prove the invertibility of $\mathcal{T}$ in Theorem 3.3 of [9]. This is important, since it shows that the recovery of n_e is unique upon inversion of $\mathcal{T}$, and hence there are no artifacts in the reconstruction due to null space.

In [21], we present new joint reconstruction and regularization techniques inspired by ideas in microlocal analysis and lambda tomography, for the simultaneous reconstruction of μ_E and n_e from $R\mu_E$ and $\mathcal{T}n_e$ data. Using microlocal analysis, we show how the $R\mu_E$ and $\mathcal{T}n_e$ data sets are complimentary in terms of the image edge recovery. Following our theory, we devise a new linear least squares reconstruction scheme using lambda penalties, which we call the "JLAM" method. The lambda penalties work by enforcing a similarity in the locations and directions of the image edges of μ_E and n_e, and hence stabilize the edge recovery in the least squares solution. For example, let us consider the reconstruction of the n_e and μ_E phantoms shown in Figure 3. The phantoms consists of a water ellipsoid, a sulfur ellipsoid, a calcium sulfate ($CaSO_4$) right-angled triangle and a thin film of titanium dioxide (TiO_2) in the shape of a cross. The density ratio of the materials that compose the n_e phantom is approximately $1:2:3:4$ (H_2O : S : $CaSO_4$: TiO_2), and the density values used are taken from the NIST database [22], with the background density (≈ 0) set to the density of dry air (near sea level). The μ_E phantom was simulated similarly, for $E = 100$ keV. The materials considered are widely used in practice. For example $CaSO_4$ is used in the production of plaster of Paris and stucco (a common construction material) [23], and TiO_2 is used in the making of decorative thin films (e.g., topaz) and in pigmentation [24].

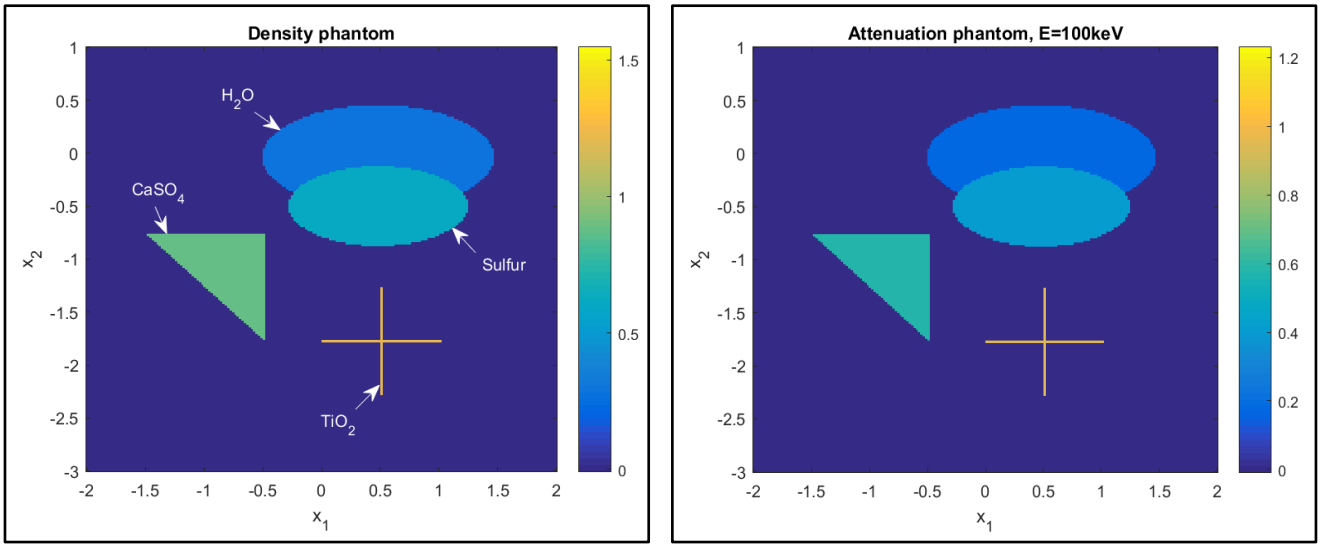

Figure 3: Density (left) and attenuation coefficient (right) phantoms. The associated materials are labelled in each case.

In Figures 4, 5 and 6, we present reconstructions of the n_e and μ_E phantoms from simulated noisy data (using additive Gaussian noise) using separate data with total variation (TV) (a well-studied state-of-the-art edge-preserving regularizer) [25], JLAM and the methods of [25] from the literature, specifically the linear poarallel level sets (LPLS) method. In Figure 4 we see severe artifacts in the reconstruction due to limited data, and the TV regularizers fail to combat the artifacts effectively. In Figure 5, we see an almost complete removal of the artifacts, and the lambda regularizers successfully preserve the edge map of the density. We see a further improvement using LPLS. See Figure 6. While the edge recovery using LPLS and JLAM is comparable, the smoothing properties of LPLS are most optimal, yielding a higher signal-to-noise ratio. In both cases (Figures 5 and 6), the joint reconstruction methods performed well, and significantly improved upon the image quality of Figure 4, using TV with separate data. Given the linearity of JLAM, the ideas of LPLS can be easily integrated with lambda regularization to modify the objectives of the literature and improve further the edge resolution of the reconstruction. To preserve the linearity of JLAM, we could also combine JLAM with a Tikhonov type regularizer. This may help smooth out the distortion observed in the JLAM reconstruction. We intend to pursue such ideas in future work.

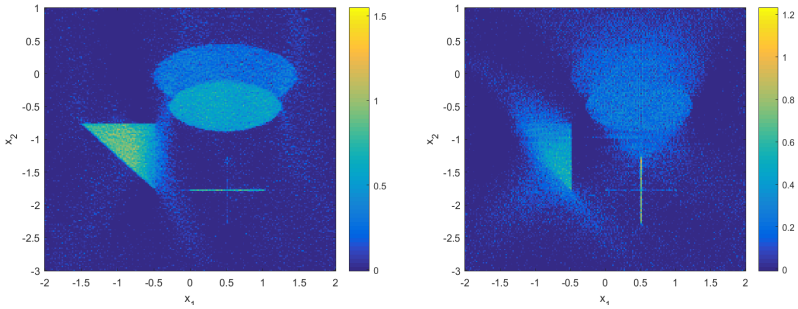

Figure 4: Density (left) and attenuation (right) phantom reconstructions using separate data and TV, with 10% Gaussian noise.

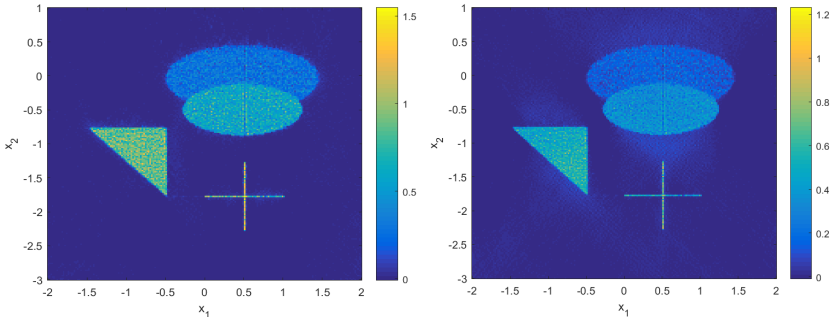

Figure 5: Density (left) and attenuation (right) phantom reconstructions using JLAM, with 10% Gaussian noise.

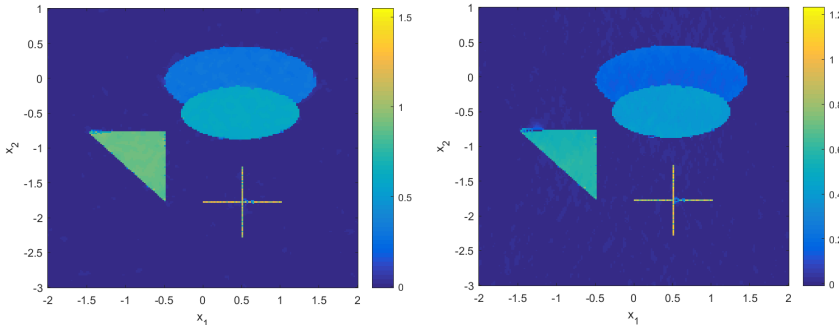

Figure 6: Density (left) and attenuation (right) phantom reconstructions using LPLS, with 10% Gaussian noise.

In addition to our peer reviewed efforts this year, following on from our work in Year 6, we completed the development of a Monte Carlo (MC) MATLAB code to simulate the Bragg, Compton and Rayleigh processes. So far we have applied our MC code to simulate data acquisition scenarios of interest to Rapiscan, and we are beginning to test the theory and inversion formulae of [8, 9, 21] using MC data. For example, let us consider the rectangular object f pictured in Figure 1. Using our MC code, we can simulate energy histograms of the Bragg scattered signal from f, measured by the detector array at $\{x_2 = 1, x_3 = \epsilon\}$, for $\epsilon \approx 0.1$ (see Figure 1). The photon counts are simulated using an X-ray tube [26], with voltage $V = 150$ keV and 10^8 photons per

projection across all energies. The source is Tungsten target, which has characteristic Bremsstrahlung peaks (jumps in intensity) at 60 keV, 66 keV and 68 keV, the largest of which occurs at 60 keV. The energy bins are 3 keV width, and the detector bins are 25 mm wide. So the data is smoothed with respect to the detector coordinate. The effects due to attenuation and self-absorption were also included in the MC simulation. See Figure 7 for energy histograms corresponding to the materials $f = \text{NaCl}$ and $f = \text{Al}$. For each material, we see the intensity peaking around the largest Bremsstrahlung peak (at 60 keV), but overall the count rate is low and the data appears noisy. To reduce the noise, we could increase the count rate per projection. However this would require a longer scanning time, which is undesirable, as we wish to scan in real-time. Hence, based on these experiments, we can anticipate a high noise level in the Bragg data. With this in mind, in future work, we aim to develop practical reconstruction algorithms in BST (based on the inversion formulae of [8]) with sufficient regularization to combat the noise.

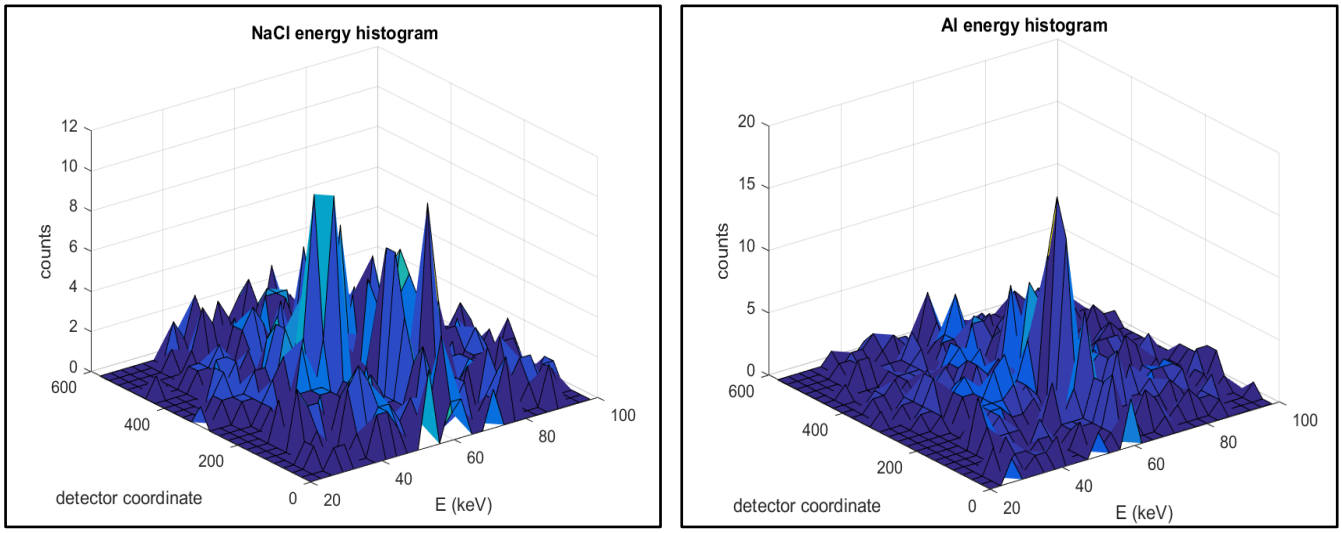

Figure 7: NaCl (left) and Al (right) energy histograms of the Bragg signal.

B.2. Optical Image Processing

The camera and optics used in the prototype required nine focal stacks arranged in a 3×3 grid to cover a $1'' \times 1''$ area. The camera and optics were mounted on a motorized XYZ stage capable of micrometer movement. Control of the prototype is done via a connected laptop PC through a LabVIEW interface.

As shown in Figure 8, the PCFIS prototype is a reflected-light dark-field microscope, where the light collected by the objective has been reflected from the specimen and not transmitted through it [27], and where the specimen is illuminated at an oblique angle such that direct, nondiffracted rays are not collective by the objective [28]. An assumption we make is that the surface diffracts less light that the particles, and so particles will appear bright in a dark field. This was the case in the four types of

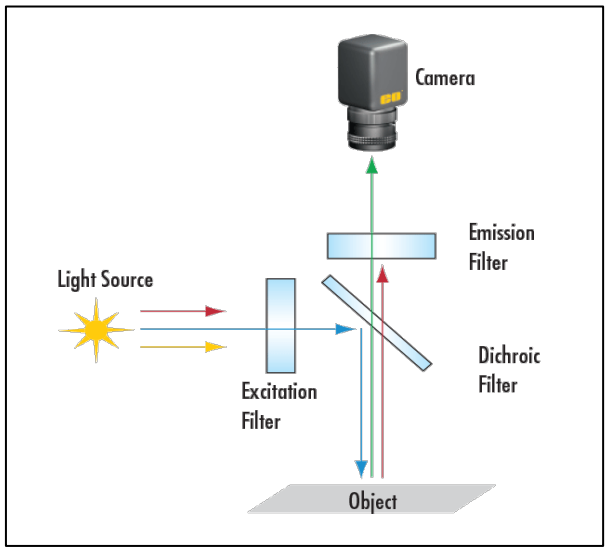

Figure 8: Schematic of dark-field microscopy.

surfaces we tested with (aluminum-coated glass, CD-ROM, curved aluminum, curved glossy black car panel).

Figure 9 shows the state diagram for the autonomous operation of the PCFIS, which uses the algorithms written by Tufts. The upper half of the diagram comprise the data collection, topography estimation, and location of potential threat particles. The lower half, circled in red, is the loop where the system analyzes a subset of the potential threat particles. In the rest of this section, we describe the data collected and the algorithms circled in blue.

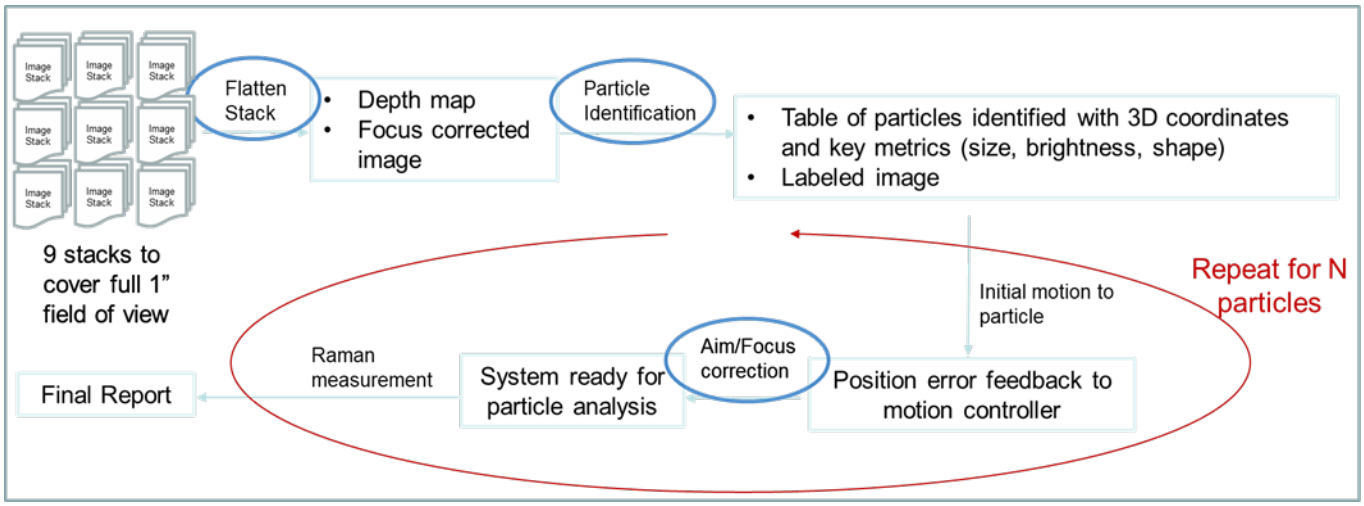

Figure 9: State diagram for the autonomous feature of the PCFIS prototype. Operations circled in blue are the optical image processing components on which members of Tufts worked.

B.3. Data Collection

As illustrated in Figure 10, a focal stack is a sequence of images of the same scene but varying the focal plane. For a typical scene in which various objects are located at different distances from the camera, different objects will appear sharp or blurry in different layers of the focal stack. In our use case, we obtain focal stacks of the surface being interrogated, with the goal of having a sharp version of every part of the surface in at least one layer of the focal stack. Importantly, every layer in a focal stack is associated with a certain depth, as we poll the z-motion motor every time a layer is captured. We obtain nine such stacks, one for every region needed to cover the 1″ × 1″ scan area.

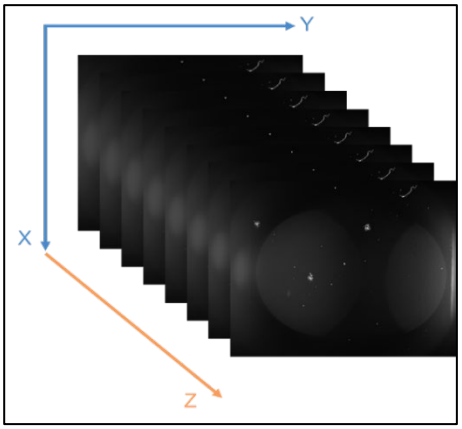

Figure 10: Example of an image stack.

B.4. Focus Stacking

We employed a technique called "focus stacking," commonly used in microscopy and macro photography to synthetically increase the depth-of-field of a camera, in order to obtain a flattened image of an arbitrary curved surface. As a byproduct of creating the flattening image, we can associate every pixel in the image (and thus every point in space) with a certain depth based on which layer in the focal stack was used to create those pixels. This is how we obtained a topography map. Whereas focus stacking algorithms have been studied before [29], to the best of our knowledge, the flattened image has always been the primary goal, and the depth information discarded. For this project, we use both.

Focus metrics evaluate how sharp an image is or how sharp different parts of an image are. Common ones used in the microscopy world can be found in this report [30]. As that paper shows, literature on the comparison between different focus metrics tend to be application-specific. For our application, we looked at a number of focus metrics listed in that paper, with our selection motivated by the need to balance algorithm time complexity and accuracy. Additionally, we explored the FISH metric found in this paper, which was interesting because of its foundation in the Discrete Wavelet Transform (DWT). The focus metric we decided on was FISH because of its vastly superior performance and acceptable computation time.

FISH was applied to images in the focus stack in a block-based fashion. For example, an image that is 1024 × 1024 is divided into blocks of 64 × 64 pixels, and each of these blocks receive a FISH score. Thus, any image to which FISH is applied is associated with a map of FISH scores as illustrated in Figure 11. To lower the computation time for the depth map, we only apply FISH to every third image in our stack with the other images are used later in the pipeline. Once we have finished applying FISH, we look at each block region and note the layer that has the maximum FISH score in that block region. The depth for this layer is assigned to every pixel in that block region.

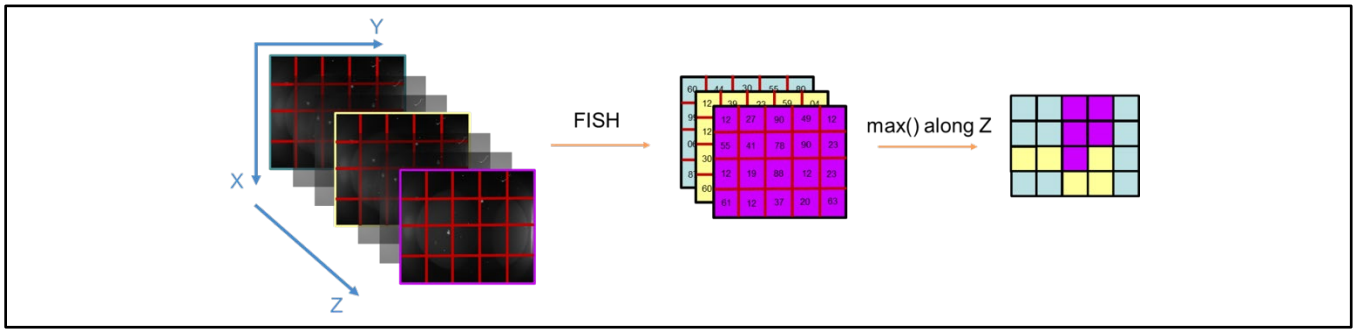

Figure 11: Block diagram of the topography estimation pipeline, using an example of a focal stack that has seven layers; a focal stack (left) where FISH is applied to the highlighted layers; maps of FISH (middle) associated with the highlighted layers; depth map (right).

To create the flattened image, we simply place the pixel in each all of the sharpest blocks next to each other. While one can identify visual artifacts with this method, the final image was fine for use in detecting particles.

B.5. Particle Detection

At its core, particle detection consists of applying a global threshold to the flattened image to obtain a binary image of the brighter portions of the image, and then performing connected component analysis on the binary image. As shown in Figure 12, a preprocessing step, called illumination normalization, seeks to remove slowly varying patterns in background illumination so that particle pixels and background pixels are well-separated in their intensities and uses a global threshold to separate particle pixels and background pixels well.

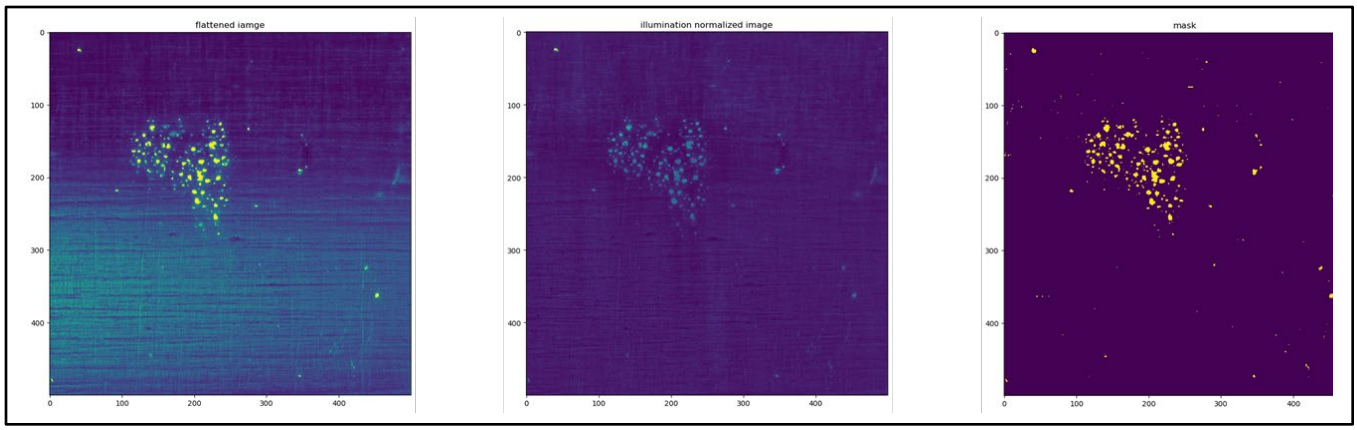

Figure 12: Intermediate images in the particle detection pipeline. Left: Flattened image, obtained from topography estimation. Middle: Illumination-normalized version of flattened image. Right: Binary mask of the previous image, which marks particle pixels.

The illumination normalization preprocessing procedure was taken from [31], which assumes the gray level is proportional to the product of the reflectance of the surface and the illumination on the scene:

$$f(x,y) = r(x,y)\, e(x,y)$$

If a logarithm transform is applied to the image, then the product becomes a sum:

$$\log f(x,y) = \log r(x,y) + \log e(x,y)$$

The method in [27] assumes first that the information on particles is contained in the reflectance, second that the illumination is slowly varying, and third that the reflectance contains high-frequency information. If so, the $\log r(x,y)$ and $\log e(x,y)$ terms are separated in the frequency domain, and we can simply apply a high-pass filter to remove the $\log e(x,y)$, leaving just the $\log r(x,y)$ term. Using the discrete cosine transform (DCT) as a frequency domain representation, the processing is illustrated in Figure 12. This is why the logarithm transform is used. Reversing the logarithm transform completes the normalization.

After illumination normalization, we can be relatively certain that brighter pixels belong to particles and darker pixels belong to the background. A shown in the rightmost part of Figure 12, we now apply a global threshold set equal to the mean pixel value plus three times the standard deviation. Finally, we apply connected component analysis to identify particle sizes, locations, and contrasts.

B.6. Aim Assist

After the motor subsystem has made its initial movement to the particle-of-interest, it is necessary to refine the position of the microscope to ensure that the Raman optics are aligned with the particle of intertest, in this case, the object in the green box in Figure 13. This aim assist step is split into two steps: a *Z*-correction and an *XY*-correction. As seen in Figure 14, for the *Z*-correction, the procedure is the same as that for stack flattening, except this time we use a tighter focal stack around the particle-of-interest: we use all image layers, and we restrict the *XY* dimensions to a smaller region around the particle-of-interest. The block size used is also smaller. The sharpest layer for the block in which the particle lies is the updated depth of the particle.

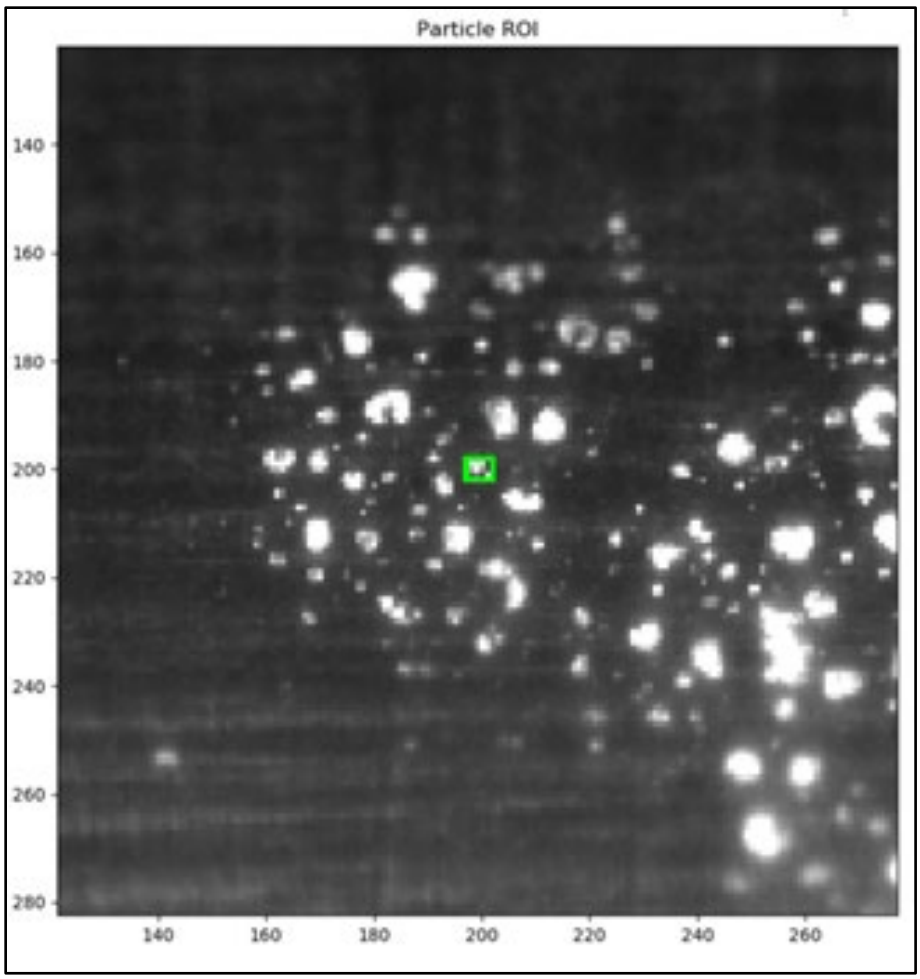

Figure 13: Template of particle and neighborhood from previous data collection.

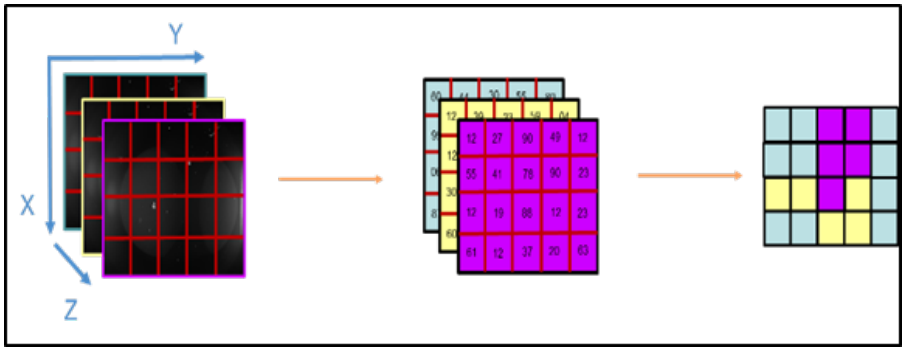

Figure 14: *Z*-correction. The focal stack is tighter in all dimensions and sampled more frequently in *Z*.

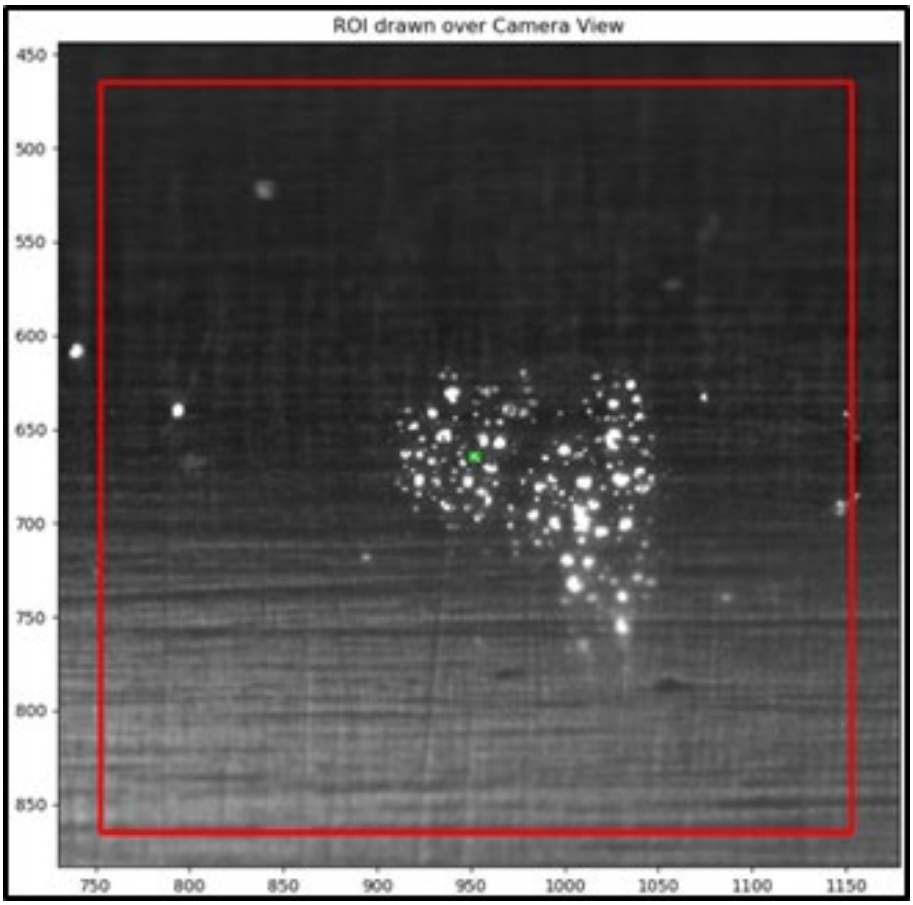

Figure 15: Optical image of the surface collected before beginning XY-refinement, zoomed-up to the particle of interest.

Subsequent to *Z* alignment, an optical image of the surface is collected for *XY* refinement; see Figure 15 for a close up of the region of interest. A 400×400 template region-of-interest around the particle to be interrogated, is then retrieved from the associated sharpest layer from the initial stack of images, see Figure 16 in this case. We create binary masks of the new and old data using the particle-finding procedure from before, then perform a template matching [32] between the new and old data to retrieve an offset by which to move the camera. The correlation surface between the template (Figure 13) and the image (Figure 15) is shown in Figure 16 where the peak at row 465 and column 753 is used to provide the shift in the optics such that the Raman spectrometer will be centered over the particle of interest.

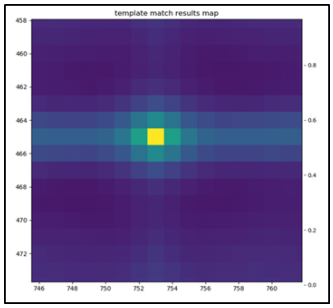

Figure 16: Template match results. Bright spot indicates location returned by algorithm.

C. Major Contributions

C.1. *X-Ray Modeling and Processing*

C.1.a. Year 7

The research advances made over the last year by the ECE group at Tufts are summarized as follows:

- Derived new injectivity theorems and explicit inversion formulae for a spindle torus Radon transform, which describes the CST problem for the RTT portal system of Figure 1. Our results were formulated as a research article [9], which is now published in the Journal of *Inverse Problems*.
- The derivation of new microlocal theorems for the CST problem in the RTT geometry. We developed a novel joint reconstruction and lambda regularization scheme to combat the image artifacts predicted by our microlocal theory. Our results have been formulated as a research article [21], which has been accepted to the journal *Inverse Problems special issue on Modern Challenges in Imaging*. The feedback from the reviewers has been highly positive and we expect publication.
- In recent work, we proposed new physical models for the Bragg scattered signal in the RTT geometry, which has led to the analysis of a new class of Radon transforms in BST. So far we have proven the invertibility of the BST transform and shown how to choose the machine parameters so as to optimize the problem stability. Our results have been formulated as a research article [8], which is under review *at The Journal of Inverse Problems and Imaging*.
- Completed the development of a novel single-scatter MATLAB code for the simulation of the Bragg, Rayleigh and Compton scattered signal. This is currently being used to test our inversion algorithms in BST and CST, and further to simulate data acquisition scenarios of interest to Rapiscan (e.g., to simulate photon counts).
- During Year 6, we worked with Prof. Eric Todd Quinto from the Department of Mathematics at Tufts. Our research focused on a novel microlocal analysis of a toric section transform, arising from a two dimensional CST problem, based on an old RTT design (with rings of sources and detectors, as opposed to the square array of Figure 1). Our results [33] have been published in the *SIAM Journal on Imaging Sciences* (*SIIMS*).
- Communicated our research at academic conferences. For example, at the Cormack Conference on Modern Challenges in Imaging, mini-symposium on security applications (August 5–9, 2019, Tufts University, Medford, MA USA), and the IS&T International Symposium on Electronic Imaging, mini-symposium on computational imaging (January 26–30, Burlingame, CA USA).
- We are now studying the microlocal and stability properties of the BST problem. So far we have derived sufficient conditions for the Bolker assumption, and shown that the RTT geometry satisfies such conditions. Satisfaction of the Bolker assumption implies that the BST inversion is stable and there are no nonlocal artifacts in the reconstruction due to the machine geometry.

C.1.b. Year 6

The Tufts PhD student supported for four years by ALERT, Ms. Hamideh Rezaee, successfully defended her doctoral dissertation and published a paper in the IEEE Transactions on Computational Imaging, on the model-based fusion of attenuation and scatter X-ray data for the joint recovery of electron density and photoelectric absorption. In support of our growing collaboration with Rapiscan Systems (Drs. Ed Morton and Dan Strellis), we began the development of new Monte Carlo (MC) software for the simulation of the

transmitted and scattered signal from randomly orientated crystalline lattices (powders) and amorphous materials. This provided valuable insight to our collaborators at Rapiscan on the expected photon counts and imaging capabilities of a new RTT portal scanner developed by the company. We developed new inversion formulae in Compton Scattering Tomography (CST), based on the RTT geometry.

C.1.c. Year 5

In the process of writing a manuscript detailing the processing method developed by our group under support from ALERT, we were asked by the reviewers of the paper to test the approach on data sets more realistic than those employed to date. To meet this need, we considered (a) the generation of data with Poisson statistics based on the single scatter model used in the processing (i.e., model matched data), as well as (b) the creation of data using sophisticated Monte Carlo codes (specifically, GEANT4) that in essence contain "all" of the physics that would be seen in experimentally obtained data. We developed a collaboration with Dr. Peter Rothschild of Heuresis Corporation to generate the Monte Carlo simulation data for a number of test scenarios. The effort of generating the data and reducing it to a form that can be input to our algorithms took most of Fall 2017 and Winter 2018. We focused on the processing of the Poisson and Monte Carlo data. Initial results demonstrated that even within the context of severely limited view geometries, our formulating of the imaging problems clearly demonstrates that the addition of scatter data to the processing provides significant benefits in terms of recovering the density relative to attenuation-only data sets. It is likely that accurate recovery of the photoelectric signature will not be possible in this data acquisition scenario. We hypothesize that sparse angle data (i.e., data acquired from a small number of angles but fully encircling the object) should yield much improved performance.

C.1.d. Year 4

The initial image formation method developed in Year 3 has been refined, as we have tested the approach on test cases far more complex than those considered during Year 3. Specifically, we have achieved the objectives in Year 4 that were outlined in the Year 3 project report. First, we have developed an objective method based on the discrepancy principle for choosing the regularization parameters defining the cost functions used as the basis for estimating both the mass density and photoelectric (PE) images from X-ray observations. Second, we have augmented the Compton data with energy resolved attenuation data and demonstrated the gain achieved from the fusion of these two data types. Finally, building on our prior efforts in multi-energy CT, we have developed a method for stabilizing the recovery of the PE image, which is based on the use of an NLM regularization scheme.

C.1.e. Year 3

We have demonstrated a method for joint recovery of both density as well as the photoelectric coefficient from severely limited view, multi-energy Compton scatter data. The overall approach is based on a variational formulation of the imaging problem. Physical intuition has guided the specific method used to solve this problem. Initial results on simulated data were quite promising.

C.1.f. Year 2

We have developed a tractable, analytical model capable for X-ray scattering and attenuation. The model has been instantiated in the form of a MATLAB-based code that will be made accessible to the broader DHS community. We believe that the model can be used effectively and efficiently in the context of image reconstruction methods seeking to recover spatial maps of electron density and photoelectric absorption information from limited view, multi-energy X-ray data.

C.1.g. Year 1

Our initial efforts under Phase 2 of ALERT support was the development of a computational forward model for multi-energy, limited view X-ray scanner modeled on the AS&E CANSCAN system, the limited view system that formed the basis for the 13-05 project. At the start of Year 2, we decided to move away from this absorption-only model as we began to explore the potential for scattered photon data to address the many challenges associated with the processing of limited view information.

C.2. Optical Image Processing

Year 7: We have designed, implemented. and transitioned to the Pendar PCFIS system the following:

- A topography estimation algorithm based on measuring the sharpness in different areas of a focal stack
- A particle detection method that returns particle coordinates within a confined search space and provides particles statistics, and that is robust against surfaces with uneven background illumination
- An aim assist method to facilitate the autonomous execution of particle identification using a Raman spectroscopy subsystem

D. Milestones

D.1.X-Ray Modeling and Processing

- **Milestone 1—Month 2:** Complete preliminary analytical model of the RTT XRD geometry with sources, detectors, collimators, and tunnel defined.
  - **Status:** Complete 08/2019
  - **Next steps:** Model is being used in development of advanced image formation methods
- **Milestone 2—Month 3:** Complete first Monte Carlo simulations of both idealized Bragg and Compton scattering spectra projected on a 2-D energy resolving detector.
  - **Status:** Complete 09/2019
  - **Next steps:** Model is being used to generate simulated data for use in exploration of the performance of image formation methods
- **Milestone 3—Month 4**: Complete more realistic Monte Carlo simulations of Bragg and Compton scattering spectra (including Poisson noise, detector energy resolution).
  - **Status:** Completed 09/2019
  - **Next steps:** The work here was basically folded into the previous milestone. Because of the Monte Carlo nature of the model, there was no need to simulate Poisson statistics. Detector energy resolution was included in the model.
- **Milestone 4—Month 5:** Complete realistic Monte Carlo simulations of Bragg and Compton scattering spectra (including scatter from system features like tunnel, belt, and detector structure).
  - **Status:** Never started
  - **Next steps:** As described previously in this report, the Tufts and Rapiscan team felt that the Monte Carlo model developed under Milestones 2 and 3 would be enough for the work to be done by Tufts for Milestones 6 and 7.

- **Milestone 5—Month 6:** Report with results from the Monte Carlo simulations supporting the detector, source, and collimator geometry for the Preliminary Design Review with DHS S&T.
  - **Status:** Never started
  - **Next steps:** As described previously in this report, the Tufts and Rapiscan team felt that the Monte Carlo model developed under Milestones 2 and 3 would be enough for the work to be done by Tufts for Milestones 6 and 7.
- **Milestone 6—Month 8:** Development and validation using both Monte Carlo and RTT data of Bragg tomography and threat classification techniques, combining Bragg scattering models with machine learning classification (e.g., neural network architectures or support vector machines).
  - **Status:** 90% complete. The Tufts team has developed the analytical foundations for a fundamentally new class of methods for the processing of Bragg scatter data collected in the "Venetian blind" sensor configuration of the Rapiscan RTT system. Also, within the context of the Rapiscan RTT geometry, the group at Tufts has developed a unique method for fused image formation from absorption and incoherent scatter data. The formal, microlocal analysis of this approach clearly explains the performance gains associated with this physics-based fusion scheme. The practical algorithm for producing images from data employs a new edge-preserving regularization method scheme for multiparameter inverse problems that produces state of the art results at substantially reduced computational load. This method promises wide applicability for problems and in fields well beyond those of interest in this project.
  - **Next steps:** We have chosen to delay the consideration of machine learning methods until such a time as we have developed a single algorithm for fusing diffraction, attenuation, and scatter X-ray data. Only when we are able to fuse all three of these data types can we best quantify the ultimate performance of X-ray methods for materials characterization.
- **Milestone 7—Month 12:** Development, validation using both Monte Carlo and RTT data and transition of materials characterization methods attenuation data, coherent scatter, and incoherent scatter. The effort will bring together microlocal analysis ideas for handling the incoherent scatter as well as iterative methods for processing the attenuation and Bragg data.
  - **Status:** In progress
  - **Next steps:** This work started in May 2020 and continued throughout the summer of 2020.

D.2. Optical Image Processing

- Enhanced machine vision processing for VICTOR Systems.
  - **Milestone 1—Month 2:** Development and use of an extended set of training data for identification of regions of interest across a broader array of luggage items.
    - **Status:** Never started
    - **Next steps:** The failure of the MODEx program to move beyond Phase I obviated this effort.
  - **Milestone 2—Month 5:** Multi-camera, video-based identification and tracking of luggage items moving along a conveyor belt.
    - **Status:** Never started
    - **Next steps:** The failure of the MODEx program to move beyond Phase I obviated this effort.

- Depth from defocus processing for Pendar PCFIS system.
  - **Milestone 1—Month 6:** Determination of technical specifications of Pendar problem and Selection of candidate depth from defocus processing methods to address Pendar problem.
    - **Status:** 07/2019
    - **Next steps:** Results of this effort formed the basis for Milestones 2–5
  - **Milestone 2—Month 7:** Implementation of candidate methods.
    - **Status:** Completed 09/2019
    - **Next steps:** Results of this effort formed the basis for Milestones 3–5
  - **Milestone 3—Month 9:** Collection of data and evaluation of processing methods.
    - **Status:** Completed 1/2020
    - **Next steps:** None
  - **Milestone 4—Month 10:** Implementation of particle detection and location algorithm. Python code tested on depth-corrected PCFIS images.
    - **Status:** Completed 10/2019
    - **Next steps:** None
  - **Milestone 5—Month 12:** Implementation of image tracking algorithm to follow particle locations as the instrument is aimed successively to the different particles. Python code uses depth corrected PCFIS images and produces updated particle coordinates as an output. The updated are used by the Pendar's motion controller to fine adjust the system aim and focus. Algorithm integrated and tested into PCFIS system.
    - **Status:** Completed 11/2019
    - **Next steps:** None

E. Final Results at Project Completion (Year 7)

E.1. Activities Toward Transition

E.1.a. X-Ray Modeling and Processing

As a result of the work discussed previously in this report, Tufts and Rapiscan submitted a white paper for consideration in response to the DHS LRBAA Securing Borders Research Area, Topic SEC BORD 04-02, Actionable Intelligence Gathering and Sharing. We proposed a three-year effort to develop, validate, and transition to fielded systems algorithms for processing X-ray attenuation and scatter data with the goal of detecting opioids and other illicit narcotics. Fusing attenuation, Compton scatter, and Bragg diffraction data, our proposed algorithms would significantly enhance CBP's abilities in terms of automated opioid and narcotics detection and confirmation. Unfortunately, DHS chose to not support this effort.

Prior to this proposal, ALERT funding at Tufts was dedicated to the development and validation of advanced computational models and associated processing methods for materials identification from X-ray data in support of the growing interests of DHS in fielding scanners at the checkpoint with few, fixed sources and detectors. Of specific interest has been the use of energy resolved observations of both attenuation and incoherently scattered photons for mapping the two physical properties to which X-rays are most sensitive

over the range of energies associated with the scanners currently under development: electron density and photoelectric attenuation coefficient. As a result of the investment by ALERT in the initial computational models and iterative reconstruction methods was a funded BAA 13-05 proposal (HSHQDC-15-C-B0012 Advanced Material Discrimination: Multi-View/Multi-Energy, Limited View, Compton Scatter Tomography) between Tufts and AS&E. That project resulted in the construction of a testbed for collection of experimental data that in turn provided for the validation of our computational models as well as initial image formation results. This effort clearly demonstrated the potential practical utility of scatter data for improving the quantitative accuracy of formed images in the context of the fixed source / detector scanners to be deployed at the checkpoint for which alternate, state of the art processing methods would be insufficient. A direct outcome of the 13-05 effort was the transition of the codes and documentation for the models and algorithms developed at Tufts to the engineers and scientists at AS&E.

E.1.b. Optical Image Processing

The optical image processing pipeline has been transitioned into the Pendar PCFIS. The collaboration between the Tufts team and Pendar greatly accelerated the identification and testing of candidate algorithms to be tested for PCFIS. The broad experience and knowledge base of the Tufts team was used to identify best options to address PCFIS challenges and issues as they emerged, making our team very reactive and greatly reducing both technical and scheduling risk for this effort.

E.2. Final Outputs Realized

E.2.a. X-Ray Modeling and Processing

- Derived new injectivity theorems, microlocal theorems, and explicit inversion formulae for a spindle torus Radon transform, which describes the Compton Scatter Tomography (CST) problem for the Rapiscan RTT portal system. Based on this work, developed a novel joint reconstruction and lambda regularization scheme to combat the image artifacts predicted by our microlocal theory. Extending and enhancing this algorithm for use in CBP-relevant problems is one component of the Rapiscan-Tufts LRBAA proposal.
- Studied the microlocal and stability properties of the Bragg scatter tomography (BST) problem. Derived sufficient conditions for the Bolker assumption, and shown that the RTT geometry satisfies such conditions meaning that that the BST inversion is stable and there are no nonlocal artifacts in the reconstruction due to the machine geometry.
- Demonstrated a method for joint recovery of both density as well as the photoelectric coefficient from severely limited view, multi-energy Compton scatter data. The overall approach is based on a variational formulation of the imaging problem. Physical intuition has guided the specific method used to solve this problem.
- Developed a tractable, analytical model capable for X-ray scattering and attenuation. The model has been instantiated in the form of a MATLAB-based code that can be made accessible to the broader DHS community.
- Transition of the codes and documentation for the models and algorithms developed at Tufts under 13-05 to the engineers and scientists at AS&E.

E.2.b. Optical Image Processing

- Development and validation of image processing pipeline for (a) identification of particles on curved surfaces from image stacks and (b) improved targeting of Rama spectral sensor.
- Implementation and transition of pipeline to Pendar PCFIS.

E.3. Results Documenting Impact

- Journal articles
  - Webber, J.W., & Miller, E.L. "Compton Scattering Tomography in Translational Geometries." *Inverse Problems*, *36*(2), 23 January 2020. https://doi.org/10.1088/1361-6420/ab4a32.
  - Webber, J.W., & Quinto, E.T. "Microlocal Analysis of a Compton Tomography Problem." *SIAM Journal on Imaging Sciences*, *13*(2), 2020, pp. 746-774. https://doi.org/10.1137/19M1251035.
  - Webber, J.W., Quinto, E.T., & Miller, E.L. "A Joint Reconstruction and Lambda Tomography Regularization Technique for Energy-Resolved X-Ray Imaging." *Inverse Problems*, special issue on modern challenges in imaging, *36*(7), 19 June 2020. https://doi.org/10.1088/1361-6420/ab8f82.
  - Webber, J.W., & Miller, E.L. "Bragg Scattering Tomography." *Inverse Problems and Imaging*, under review. Arxiv preprint available at https://arxiv.org/abs/2004.10961.
  - Rezaee, H., Rothschild, P., Tracey, B., & Miller, E.L. "On the Fusion of Energy Resolved Scatter and Attenuation Data for Limited-View X-Ray Materials Characterization with Application to Security Screening." *IEEE Transactions on Computational Imaging*, *5*(4), December 2019, pp. 620-634. DOI: 10.1109/TCI.2019.2909858.
  - Desmal, A., Schubert, J.R., Denker, J., Kisner, S.J., Rezaee, H., Couture, A., Miller, E.L., & Tracey, B.H. "Limited-View X-Ray Tomography Combining Attenuation and Compton Scatter Data: Approach and Experimental Results." *IEEE Access* 7, 2019, pp. 165734-165747. https://doi.org/10.1109/ACCESS.2019.2953217.
- Successful 13-05 project with AS&E including transition of code from Tufts to AS&E
- Successful development and transition into Pendar product of an image processing pipeline for particle identification and Raman spectral microscope target localization
- Current LRBAA proposal effort between Tufts and Rapiscan

III. RELEVANCE AND TRANSITION

A. Relevance of Research to the DHS Enterprise

Both the X-ray and optical components of this project share a common relevance to the homeland security enterprise: namely the development and fielding of sophisticated sensor systems and embedded processing methods for the detection of explosive materials at the checkpoint. Current methods for luggage scanning at the checkpoint are insufficient to meet the future needs and expectations of the traveling public as well as the rapidly emerging and changing threats facing the United States. All viable solutions to this problem are based on the deployment of advanced sensing systems. The success of such systems in turn is driven both by the physical processes being exploited to detect and characterize explosive materials embedded in cluttered environments as well as the processing methods designed to turn sensor data into actionable information.

Meeting the performance specifications set by the Department of Homeland Security requires the exploitation of increasingly subtle physical effects that in turn leads to data whose reliable interpretation is made all the more challenging not only due to noise, but also systematic effects associated with the physics of the sensor coupled with uncertainty in the environment. In the context of the Pendar system for example (a similar case could be made for the Rapiscan project), the spectral signature of a compound of interest changes dramatically as a function of its concentration as well as the surface on which it has been deposited. Both of these complications are essentially uncontrolled in this application thereby rendering useless any sort of "off-the-shelf" processing method. The success of the overall system then requires a carefully designed and very deliberative approach to integrating the engineers and scientists responsible for the processing with those constructing the sensor itself. Over the past seven years, the group at Tufts has pursued just this type of collaboration both with Pendar and AS&E/Rapiscan Systems and, as discussed below have successfully transitioned technologies from academia to our HSE-serving industrial partners.

We are seeking to address challenges associated with automated scanning and threat detection in both checked luggage and baggage that is inspected at checkpoints. The overall goal is to determine spatial maps of material properties in an automated manner from multi-energy X-ray data collected in limited-view types of geometries or optical methods. Any metric that quantifies the accuracy of the material maps can be used to evaluate the performance of our work including:

- Confusion matrices capturing the percentage of correctly and incorrectly labeled pixels for scenarios where ground truth is known.
- If one is concerned with purely binary problems (threat object versus all other types of materials), then the receiver operating characteristic, plotting detection probabilities versus false alarm rates, could be developed.
- Finally, we could visualize accuracy using uncertainty cloud analysis developed as part of ALERT Task Order 3 and employed in "Stabilizing Dual-Energy X-Ray Computed Tomography Reconstructions Using Patch-Based Regularization" by Brian H. Tracey and Eric L. Miller [*Inverse Problems*, *3*(10), 2015, 105004]. These clouds would plot the average value and first standard deviation ellipse of the distribution of photoelectric and electron density over known target regions in our reconstructions. In comparing multiple candidate processing methods, smaller ellipses and means closer to ground truth are indicators of higher accuracy.

B. Status of Transition at Project End

B.1. X-Ray Modeling and Processing

As a result of the work discussed previously in this report, Tufts and Rapiscan have submitted a white paper for consideration in response to the DHS LRBAA Securing Borders Research Area, Topic SEC BORD 04-02, Actionable Intelligence Gathering and Sharing. We have proposed a three-year effort to develop, validate, and transition to fielded systems algorithms for processing X-ray attenuation and scatter data with the goal of detecting opioids and other illicit narcotics. Fusing attenuation, Compton scatter, and Bragg diffraction data, our proposed algorithms will significant enhance Customs and Border Protection's abilities in terms of automated opioid and narcotics detection and confirmation.

B.2. Optical Image Processing

The optical image processing pipeline has been transitioned into the Pendar PCFIS. The collaboration between the Tufts team and Pendar greatly accelerated the identification and testing of candidate algorithms

to be tested for PCFIS. The broad experience and knowledge base of the Tufts team was used to identify best options to address PCFIS challenges and issues as they emerged, making our team very reactive and greatly reducing both technical and scheduling risk for this effort.

C. Transition Pathway and Future Opportunities

C.1. X-Ray Modeling and Processing

This project was a close collaboration between the Tufts team of Dr. Miller and Dr. Webber and the Rapiscan team of Dr. Strellis and Dr. Morton. The group had a teleconference about twice a month to review progress on the project, ensure relevance of the Tufts effort to Rapiscan, and set goals for the next time period. The work being performed at Tufts benefitted Rapiscan by providing a collaboration whereby academia was able concentrate on the exploration of new methods and data extraction processes while allowing Rapiscan participants to concentrate on the application of the technology. Throughout this collaboration, Rapiscan has provided laboratory X-ray diffraction data for Tufts to use in benchmarking their methods. Tufts has provided valuable feedback on the data Rapiscan has provided and has suggested new measurements or materials where new data would be valuable.

The LRBAA proposal represents one future opportunity being pursued. Additionally, the Tufts group will seek to collaborate with Rapiscan in response to any new RFPs released by DHS looking for advanced methods for collecting and processing X-ray data.

C.2. Optical Image Processing

This project is a close collaboration between the Tufts team of Dr. Miller and Mr. Yau and the Pendar team led by Dr. Blanchard. Mr. Yau, hired by Tufts to work on this project, was physically located at Pendar interacting on a continual basis with the PCFIS team. Dr. Miller and Mr. Yau met weekly to discuss progress on the project, address technical issues in need of solution, and set goals for the upcoming week. Prior to programmatic deadlines associated with the PCFIS system, Dr. Miller visited Pendar to provide additional technical support.

The Tufts group will seek to collaborate with Pendar in response to any new RFPs released by DHS looking for advanced methods for collected and processing optical data.

D. Customer Connections

- At Rapiscan: Dr. Dan Strellis and Dr. Ed Morton. We meet with both Dr. Strellis and Dr. Morton once every two weeks to review progress on our project and plan for future efforts.
- At Pendar: Dr. Romain Blanchard. We speak with Dr. Blanchard approximately monthly concerning progress on this project.

IV. PROJECT ACCOMPLISHMENTS AND DOCUMENTATION

A. Peer Reviewed Journal Articles

1. Rezaee, H., Rothschild, P., Tracey, B., & Miller, E.L. “On the Fusion of Energy Resolved Scatter and Attenuation Data for Limited-View X-Ray Materials Characterization with Application to Security Screening.” *IEEE Transactions on Computational Imaging*, *5*(4), December 2019, pp. 620–634. https://doi.org/10.1109/TCI.2019.2909858.

2. Webber, J.W., & Miller, E.L. "Compton Scattering Tomography in Translational Geometries." *Inverse Problems*, *36*(2), 23 January 2020. https://doi.org/10.1088/1361-6420/ab4a32.
3. Webber, J.W., & Quinto, E.T. "Microlocal Analysis of a Compton Tomography Problem." *SIAM Journal on Imaging Sciences*, *13*(2), 2020, pp. 746–774. https://doi.org/10.1137/19M1251035.
4. Webber, J.W., Quinto, E.T., & Miller, E.L. "A Joint Reconstruction and Lambda Tomography Regularization Technique for Energy-Resolved X-Ray Imaging." *Inverse Problems*, special issue on modern challenges in imaging, *36*(7), 19 June 2020. https://doi.org/10.1088/1361-6420/ab8f82.

Pending –

1. Webber, J.W., & Miller, E.L. "Bragg Scattering Tomography." Under review at *Inverse Problems and Imaging*. Arxiv preprint available at https://arxiv.org/abs/2004.10961.

B. Other Conference Proceedings

1. Webber, J.W., Quinto, E.T., & Miller, E.L. "A Joint Reconstruction and Lambda Tomography Regularization Technique for Energy-Resolved X-Ray Imaging." *Computational Imaging XVIII Conference* at the *IS&T Electronic Imaging 2020 Symposium*, Burlingame, CA. 26–30 January 2020.

C. Other Presentations

1. Webber, J.W. Speaker at *The Cormack Conference on Modern Challenges in Imaging*, mini-symposium on security applications. Tufts University, Medford, MA. 5–9 August 2019.
2. Webber, J.W. Speaker at *The IS&T International Symposium on Electronic Imaging*, mini-symposium on computational imaging, Burlingame, CA, 26–30 January 2020.
3. Webber, J.W. "Generalized Radon Transforms and Applications." Mini-symposium. *The 10th International Conference on Inverse Problems: Modelling and Simulation*, Malta. 24–30 May 2020.
4. Webber, J.W., & Miller, E.L. Co-organizers of "Scattering Tomography and Generalized Radon Transforms," mini-symposium at *SIAM Conference on Imaging Sciences*, Toronto, Canada, 6–9 July 2020.

V. REFERENCES

[1] G. J. Edelman, E. Gaston, T. G. van Leeuwen, P. J. Cullen, and M. C. G. Aalders, "Hyperspectral imaging for non-contact analysis of forensic traces," (in English), *Forensic Sci Int,* vol. 223, no. 1-3, pp. 28-39, Nov 30 2012, doi: 10.1016/j.forsciint.2012.09.012.

[2] D. S. Moore, "Instrumentation for trace detection of high explosives," *Review of Scientific Instruments,* vol. 75, no. 8, pp. 2499-2512, 2004, doi: 10.1063/1.1771493.

[3] P. I. Hendricks et al., "Autonomous in Situ Analysis and Real-Time Chemical Detection Using a Backpack Miniature Mass Spectrometer: Concept, Instrumentation Development, and Performance," (in English), *Anal Chem,* vol. 86, no. 6, pp. 2900-2908, Mar 18 2014, doi: 10.1021/ac403765x.

[4] W. R. de Araujo et al., "Portable analytical platforms for forensic chemistry: A review," (in English), *Analytica Chimica Acta,* vol. 1034, pp. 1-21, Nov 30 2018, doi: 10.1016/j.aca.2018.06.014.

[5] "Virsa™ Raman Analyser." https://www.renishaw.com/en/virsa-raman-analyser--44980.

[6] D. F. Swinehart, "The beer-lambert law," *Journal of chemical education,* vol. 39, no. 7, p. 333, 1962.

[7] A. C. Kak, M. Slaney, and G. Wang, "Principles of computerized tomographic imaging," *Medical Physics,* vol. 29, no. 1, pp. 107-107, 2002.

[8] J. Webber and E. Miller, "Braggh Scatter Tomography," *Inverse Problems and Imaging,* 2020.

[9] J. Webber and E. L. Miller, "Compton scattering tomography in translational geometries," (in English), *Inverse Probl,* vol. 36, no. 2, Feb 2020, doi: ARTN 025007, 10.1088/1361-6420/ab4a32.

[10] F. Natterer, *The mathematics of computerized tomography*. SIAM, 2001.

[11] J. J. DeMarco and P. Suortti, "Effect of Scattering on the Attenuation of X Rays," *Physical Review B,* vol. 4, no. 4, p. 1028, 1971.

[12] A. J. C. Wilson and V. Geist, "International Tables for Crystallography. Volume C: Mathematical, Physical and Chemical Tables. Kluwer Academic Publishers, Dordrecht/Boston/London 1992 (published for the International Union of Crystallography), 883 Seiten, ISBN 0-792-3-16-38X.

[13] M. K. Nguyen and T. T. Truong, "Inversion of a new circular-arc Radon transform for Compton scattering tomography (vol 26, 065005, 2010)," (in English), *Inverse Probl,* vol. 26, no. 9, Sep 2010, doi: Artn 099802,10.1088/0266-5611/26/9/099802.

[14] V. P. Palamodov, "An analytic reconstruction for the Compton scattering tomography in a plane," (in English), *Inverse Probl,* vol. 27, no. 12, Dec 2011, doi: Artn 125004, 10.1088/0266-5611/27/12/125004.

[15] T. T. Truong, M. K. Nguyen, and H. Zaidi, "The mathematical foundations of 3D Compton scatter emission imaging," *International journal of biomedical imaging,* vol. 2007, 2007.

[16] F. G. Tricomi, *Integral equations*. Courier Corporation, 1985.

[17] A. Taylor and H. Sinclair, "On the Determination of Lattice Parameters by the Debye-Scherrer Method," (in English), *P Phys Soc Lond,* vol. 57, no. 320, pp. 126-135, 1945, doi: Doi 10.1088/0959-5309/57/2/306.

[18] B. E. Warren, *X-ray Diffraction*. Courier Corporation, 1990.

[19] D. Ballantine Jr *et al.*, *Acoustic wave sensors: theory, design and physico-chemical applications*. Elsevier, 1996.

[20] O. Klein and Y. Nishina, "Über die Streuung von Strahlung durch freie Elektronen nach der neuen relativistischen Quantendynamik von Dirac," *Zeitschrift für Physik,* vol. 52, no. 11-12, pp. 853-868, 1929.

[21] J. Webber, E. T. Quinto, and E. Miller, "A joint reconstruction and lambda tomography regularization technique for energy-resolved X-ray imaging," *Inverse Problems special issue on Modern Challenges in Imaging,* 2020, doi: 10.1088/1361-6420/ab8f82

[22] J. Hubbell, "Photon cross sections, attenuation coefficients and energy absorption coefficients," *National Bureau of Standards Report NSRDS-NBS29, Washington DC,* 1969.

[23] F. Wirsching, "Calcium sulfate," *Ullmann's encyclopedia of industrial chemistry,* 2000.

[24] J. Winkler, *Titanium Dioxide: Production, Properties and Effective Usage 2nd Revised Edition*. Vincentz Network, 2014.

[25] M. J. Ehrhardt *et al.*, "Joint reconstruction of PET-MRI by exploiting structural similarity," (in English), *Inverse Probl,* vol. 31, no. 1, Jan 2015, doi: Artn 015001, 10.1088/0266-5611/31/1/015001.

[26] R. Behling, *Modern Diagnostic X-Ray Sources: Technology, Manufacturing, Reliability*. CRC Press, 2015.

[27] Y. Leng, "Materials Characterization: Introduction to Microscopic and Spectroscopic Methods, 2nd Edition," (in English), *Materials Characterization: Introduction to Microscopic and Spectroscopic Methods, 2nd Edition,* pp. 1-376, 2013, doi: 10.1002/9783527670772.

[28] D. B. Murphy, *Fundamentals of light microscopy and electronic imaging*. John Wiley & Sons, 2002.

[29] M. S. Sigdel, M. Sigdel, S. Dinc, I. Dinc, M. L. Pusey, and R. S. Aygun, "FocusALL: Focal Stacking of Microscopic Images Using Modified Harris Corner Response Measure," (in English), *Ieee Acm T Comput Bi,* vol. 13, no. 2, pp. 326-340, Mar-Apr 2016, doi: 10.1109/Tcbb.2015.2459685.

[30] J. M. Mateos-Pérez *et al.*, "Comparative evaluation of autofocus algorithms for a real-time system for automatic detection of Mycobacterium tuberculosis," *Cytom Part A,* vol. 81, no. 3, pp. 213-221, 2012.

[31] W. L. Chen, M. J. Er, and S. Q. Wu, "Illumination compensation and normalization for robust face recognition using discrete cosine transform in logarithm domain," (in English), *Ieee T Syst Man Cy B,* vol. 36, no. 2, pp. 458-466, Apr 2006, doi: 10.1109/Tsmcb.2005.857353.

[32] R. Brunelli, *Template matching techniques in computer vision: theory and practice*. John Wiley & Sons, 2009.

[33] J. W. Webber and E. T. Quinto, "Microlocal Analysis of a Compton Tomography Problem," *SIAM Journal on Imaging Sciences,* vol. 13, no. 2, pp. 746-774, 2020, doi: 10.1137/19m1251035.